





PHOTONICS Research

Micropascal-sensitivity ultrasound sensors based on optical microcavities

HAO YANG,^{1,2,†} XUENING CAO,^{1,2,†} ZHI-GANG HU,^{1,2} YIMENG GAO,^{1,2} YUECHEN LEI,^{1,2} MIN WANG,^{1,2} ZHANCHUN ZUO,^{1,3} XIULAI XU,⁴  AND BEI-BEI LI^{1,3,*} 

¹Beijing National Laboratory for Condensed Matter Physics, Institute of Physics, Chinese Academy of Sciences, Beijing 100190, China

²University of Chinese Academy of Sciences, Beijing 100049, China

³Songshan Lake Materials Laboratory, Dongguan 523808, China

⁴State Key Laboratory for Mesoscopic Physics and Frontiers Science Center for Nano-optoelectronics, School of Physics, Peking University, Beijing 100871, China

[†]These authors contributed equally to this work.

*Corresponding author: libeibei@iphy.ac.cn

Received 1 February 2023; revised 18 April 2023; accepted 19 April 2023; posted 21 April 2023 (Doc. ID 486849); published 12 June 2023

Whispering gallery mode (WGM) microcavities have been widely used for high-sensitivity ultrasound detection, owing to their optical and mechanical dual-resonance enhanced sensitivity. The ultrasound sensitivity of the cavity optomechanical system is fundamentally limited by thermal noise. In this work, we theoretically and experimentally investigate the thermal-noise-limited sensitivity of a WGM microdisk ultrasound sensor and optimize the sensitivity by varying the radius and a thickness of the microdisk, as well as using a trench structure around the disk. Utilizing a microdisk with a radius of 300 μm and thickness of 2 μm , we achieve a peak sensitivity of 1.18 $\mu\text{Pa Hz}^{-1/2}$ at 82.6 kHz. To the best of our knowledge, this represents the record sensitivity among cavity optomechanical ultrasound sensors. Such high sensitivity has the potential to improve the detection range of air-coupled ultrasound sensing technology. © 2023 Chinese Laser Press

<https://doi.org/10.1364/PRJ.486849>

1. INTRODUCTION

Ultrasound has played an important role in various applications. For instance, non-destructive testing with ultrasound has been extensively employed in industrial quality inspection [1]. Ultrasound imaging can detect deeper tissue structures than light and help in medical diagnosis [2]. Additionally, ultrasound can also be applied to positioning and ranging systems [3], functioning effectively even in adverse weather conditions. Meanwhile, ultrasound detection technology is also facing several challenges. Ultrasound experiences significant loss at the interface of different media due to the acoustic impedance mismatch. Consequently, detection often necessitates an acoustic impedance-matching coupling agent to achieve high sensitivity. However, in some scenarios where coupling agents are not suitable (e.g., wounds, high temperatures, materials that cannot be damaged), air-coupled ultrasound detection becomes the optimal choice. To counteract the effects of airborne losses, air-coupled ultrasound sensors with higher sensitivity are required. Commonly used today are commercially available piezoelectric ultrasound transducers, which are produced through a mature process and easily integrated with circuits. However, to meet the high sensitivity requirements, the sizes of these transducers generally range from millimeters to centimeters, significantly reducing the spatial resolution for imaging.

To address these limitations, optical ultrasound sensors have been developed, offering both high sensitivities and spatial resolutions, such as Fabry–Perot (F-P) interferometers [4–7], whispering gallery mode (WGM) microcavities [8–22], and Bragg gratings [23,24]. Pressure changes induced by incoming ultrasound cause optical resonance shifts in these resonators, which can be optically read out with high sensitivity. F-P cavity ultrasound sensors using graphene [4] and silver films [5] on optical fibers have already achieved sensitivities in the tens of micropascals range. However, millimeter-scale dimensions are necessary for such high sensitivities. A newly designed F-P cavity, comprising a solid plano–concave polymer microcavity [6] formed between two highly reflective mirrors, has realized an equivalent noise pressure of 1.6 $\text{mPa Hz}^{-1/2}$, wide directivity, and demonstrated applications in biomedical imaging. Owing to their ultrahigh quality (Q) factor enhanced light–matter interactions, WGM microcavities [25–27] have demonstrated exceptional performance for sensing of temperature [28], gas [29], nanoparticles and biomolecules [30–38], wavelengths [39], phase-transition dynamics [40,41], etc. Various microcavity structures, such as microspheres [8–11], microrings [12–16], microbubbles [17–20], microdisks [21], and microtoroids [22], have been employed for ultrasound sensing. Among them, cavity optomechanical systems

[42–50] provide an ideal platform for ultrasound sensing due to their dual-resonance enhanced sensitivity. The sensitivity of optomechanical ultrasound sensors is fundamentally limited only by thermal noise, introduced by both the intrinsic damping of the mechanical resonator and collisions with the gas molecules around the sensor. Therefore, reaching the thermal-noise-limited regime is crucial to achieving better sensitivity. Recently, thermal-noise-limited ultrasound sensitivities on the order of micropascals have been realized [7,21,22]. Further improvement of thermal-noise-limited ultrasound sensitivity, however, still necessitates more systematic study.

In our previous work [22], we conducted a theoretical study on thermal-noise-limited ultrasound sensitivity, without considering the effects of the pressure difference between the upper and lower surfaces of the microdisk or the spatial overlap between the mechanical mode and ultrasound. In this work, we perform a more systematic study on thermal-noise-limited ultrasound sensitivity, using suspended WGM microdisks both theoretically and experimentally. Our research demonstrates that a trench structure surrounding the microdisk can increase the pressure difference, thereby enhancing its response to ultrasound. We study the trends of sensitivities with the radius and thickness of the microdisk, taking into account the pressure difference and spatial overlap. Experimentally, we fabricate microdisks with various radii and thicknesses, featuring a trench structure, and measure their sensitivities in the air across frequency ranges from tens of kHz to over 1 MHz. To the best of our knowledge, we achieve the best cavity optomechanical ultrasound sensitivity of $1.18 \mu\text{Pa Hz}^{-1/2}$ at 82.6 kHz, using a microdisk with a radius of 300 μm and a thickness of 2 μm . This exceptional sensitivity has the potential to extend the detection range of air-coupled ultrasound sensing technology, which is particularly beneficial for applications such as positioning systems and gas photoacoustic spectroscopy [51].

2. THEORETICAL ANALYSIS

Ultrasound sensitivity is limited by the noise of the sensor. In an optomechanical system, the main noise sources include thermal-mechanical noise, optical shot noise, and backaction noise from the probe light [42,45,52]. Previous studies have shown that, with a proper choice of parameters in the detection system, including optical power, optical Q factor, mechanical Q factor, and optomechanical coupling coefficient $G = d\omega/dx$ (where ω and x represent the optical resonance angular frequency and mechanical displacement, respectively), the measurement strength (the level of the thermal noise relative to the measurement noise) can be increased to enter a thermal-noise-dominant regime. This is advantageous for achieving better sensitivity. In this work, we focus on studying the thermal-noise-limited ultrasound sensitivity and optimizing the sensitivity by varying the geometric parameters of a microdisk. The thermal-noise-limited ultrasound sensitivity, P_{\min} , can be expressed as Eq. (1) [21,42],

$$P_{\min}(\omega) = \frac{1}{r\zeta A} \sqrt{2m\gamma k_B T}, \quad (1)$$

where r represents the ratio of the pressure difference between the upper and lower surfaces of the sensor to the peak pressure

at the antinode of the incident ultrasonic wave, ζ is the spatial overlap between the incident ultrasound and the mechanical displacement profile of the sensor, and A refers to the sensor area. The square root term quantifies the thermal-mechanical force spectral density. Here, m and γ are the effective mass and damping rate of the mechanical mode of the sensor, k_B is the Boltzmann constant, and T is the temperature.

This equation demonstrates how various parameters affect sensitivity. First, a higher mechanical Q factor (smaller γ) is beneficial for achieving better sensitivity. Using a microdisk with a thin silicon pedestal can reduce clamping loss, thereby increasing the mechanical Q factors. Second, better sensitivity can be achieved by employing mechanical modes with larger spatial overlaps ζ . For a microdisk ultrasound sensor, the flapping modes exhibit good spatial overlaps with the ultrasound. Therefore, in this work, we primarily focus on the flapping modes of the microdisk. Figures 1(a) and 1(b) display the normalized displacement distributions of the first- and second-order flapping modes of a microdisk (with a radius of 100 μm , thickness of 2 μm , and pedestal radius of 10 μm) obtained from the finite element method (FEM) simulations. Their spatial overlaps with the ultrasound perpendicularly incident to the microdisk are approximately 0.58 and 0.23, respectively. The spatial overlap is smaller for the second-order flapping mode, as it is related to the direction of the mechanical displacement, and the displacement cancellation in opposite directions of the second-order flapping mode reduces its spatial overlap. Their mechanical resonance frequencies are 219 kHz and 1.32 MHz, respectively.

Pressure difference is also a crucial factor that affects sensitivity, and a larger pressure difference r results in better sensitivity. The pressure difference r depends on the ultrasound frequency and the structure of the sensor. In our work, we find that the pressure difference at low frequencies can be increased by employing a trench structure around the microdisk sensor. We utilize a two-dimensional axisymmetric model to simulate the pressure distribution of the microdisk, with the axis of rotational symmetry located at the center of the microdisk. Figures 1(c) and 1(d) display the pressure distributions of the microdisk without a trench structure at the first- and second-order flapping modes, with pressure differences $r = 0.68$ and $r = 1.91$, respectively. The pressure difference is higher for the second-order flapping mode due to the increasing spatial gradient of the pressure wave at higher frequencies. Figures 1(e) and 1(f) show the pressure distributions of the microdisk with a trench structure at the first- and second-order flapping modes, with pressure differences $r = 1.35$ and $r = 1.97$, respectively. It can be observed that the trench structure significantly increases the pressure difference of the first-order flapping mode, while the pressure difference of the second-order flapping mode is not greatly affected. This is because, at lower frequencies, the trench structure can greatly enhance the ultrasonic wave reflections between the substrate and the microdisk, thereby increasing the pressure difference. However, for the second-order flapping mode, the reflection between the substrate and the microdisk is decreased due to the reduced restraint of the trench structure on acoustic waves, which results from the more pronounced diffraction at the trench structure for higher-frequency (shorter-wavelength) acoustic waves.

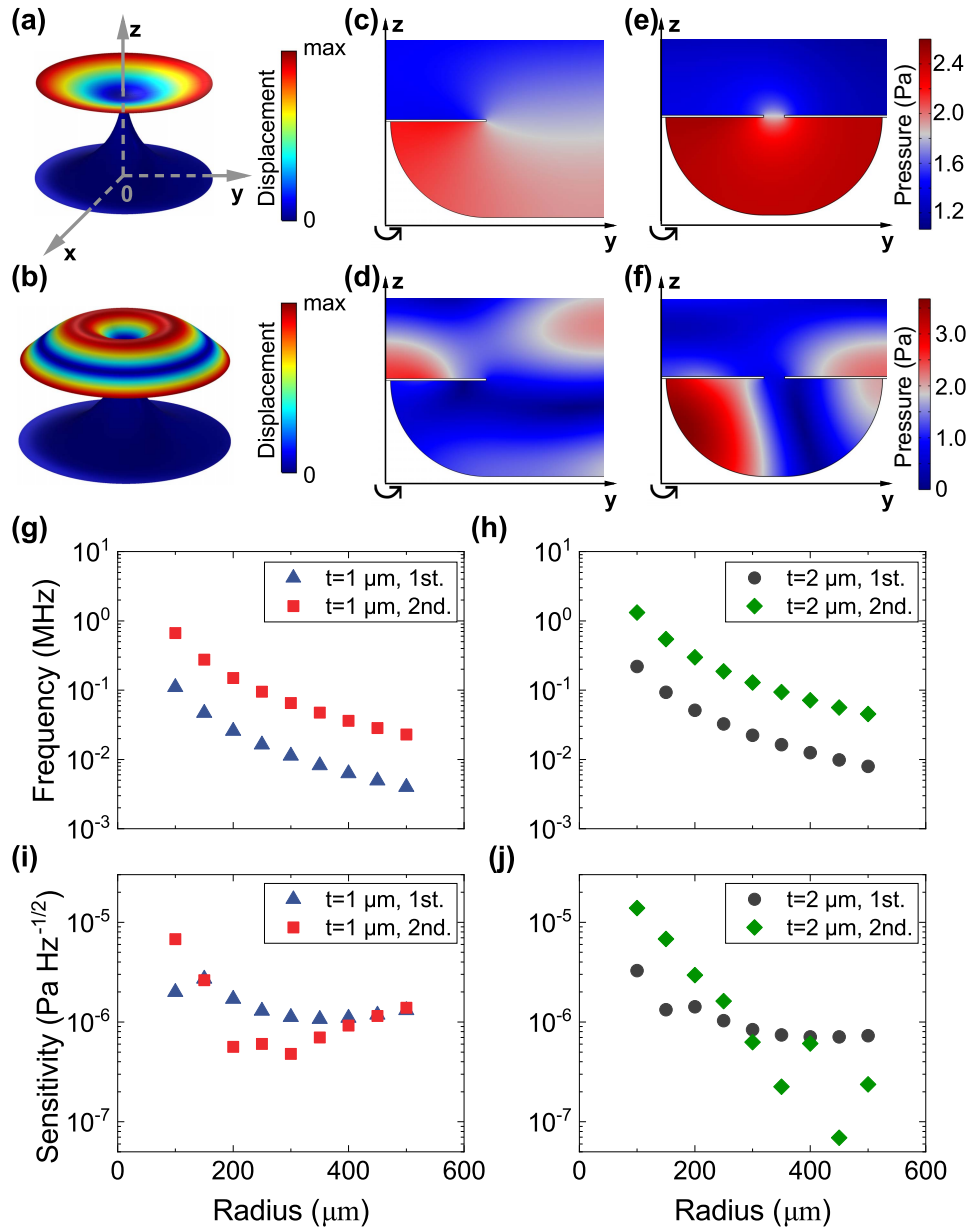


Fig. 1. (a), (b) Simulated displacement distributions of the first- and second-order flapping modes, respectively. (c)–(f) Simulated pressure distributions of the microdisk (c), (d) without and (e), (f) with the trench structure, at the frequencies of the (c), (e) first-order and (d), (f) second-order flapping modes. In the simulations of (c)–(f), we use a two-dimensional axisymmetric model, with the axis of rotational symmetry located at the center of the microdisk (z axis), indicated by the arrows at the bottom. The ultrasonic wave with a sound pressure of 1 Pa is perpendicularly incident to the microdisk from above. The microdisk used here has a radius of $100\ \mu\text{m}$ and a thickness of $2\ \mu\text{m}$. The pressure differences are (c) 0.68, (d) 1.91, (e) 1.35, and (f) 1.97, respectively. (g), (h) Simulated mechanical resonance frequencies of the flapping modes of $1\ \mu\text{m}$ thick and $2\ \mu\text{m}$ thick microdisks, respectively, as a function of the disk radius. (i), (j) Calculated sensitivities of microdisks, with thicknesses of $1\ \mu\text{m}$ and $2\ \mu\text{m}$, respectively. The blue triangles and red squares represent the results of the first- and second-order flapping modes of the microdisk with a thickness of $1\ \mu\text{m}$. The black circles and green rhombuses represent the results of the first- and second-order flapping modes of the microdisk with a thickness of $2\ \mu\text{m}$.

Equation (1) also suggests that the sensitivity improves with a larger sensor area A , but the effect of the pressure difference must also be considered. In the following, we theoretically study the ultrasound sensitivity at the first- and second-order flapping modes of microdisk sensors with different radii, taking into account the pressure difference r and spatial overlap ζ . Figures 1(g) and 1(h) display the simulated resonance

frequencies of the first- and second-order flapping modes of the microdisk as a function of the disk radius, with thicknesses of $1\ \mu\text{m}$ and $2\ \mu\text{m}$, respectively. The resonance frequency decreases with increasing radius and decreasing thickness. Therefore, achieving higher-frequency ultrasound sensing can be accomplished by reducing the radius or increasing the thickness of the microdisk, thereby increasing the

mechanical frequency to the MHz range, which is useful for applications such as photoacoustic imaging and biomedical diagnosis. We obtain the spatial overlap and pressure difference through simulation and calculate the corresponding sensitivities for microdisks with different radii and thicknesses of 1 μm and 2 μm , as shown in Figs. 1(i) and 1(j), respectively. The simulations of mechanical frequencies in Figs. 1(g) and 1(h) do not take into account the trench structures, as they do not affect the mechanical frequencies. However, the trench structures are considered in the calculations of ultrasound sensitivities shown in Figs. 1(i) and 1(j), as they affect the pressure difference of the microdisk and, thus, the ultrasound sensitivity. According to Eq. (1), the increase of the radius will increase the sensor area and, thus, improve the sensitivity. However, the decrease in the resonance frequency will hinder the improvement of the sensitivity due to the decreased pressure difference. As a result, under the effect of these two factors, the sensitivity first improves and then degrades. By comparing the first- and second-order flapping modes, it can be observed that the sensitivities of the first-order flapping mode are better for small-radius microdisks because it has a larger spatial overlap. However, when the radius becomes larger, the effect of the pressure difference increases, resulting in worse sensitivities of the first-order flapping mode.

3. DEVICE FABRICATION AND MEASUREMENT

For experimental demonstration, we fabricate a series of microdisks with various radii and thicknesses, featuring trench structures around the microdisks. The fabrication process includes photolithography, hydrofluoric acid wet etching, and xenon difluoride (XeF_2) dry etching. During the XeF_2 dry etching

process, the silicon pedestal beneath the silica microdisk is thinned to improve mechanical compliance. Meanwhile, a trench is etched around the microdisk while the rest of the silicon substrate is preserved. Figure 2(a) displays an optical microscopic image of the microdisk with a radius of 150 μm . The cross section electric field distribution of the fundamental mode close to the surface of the microdisk is shown in Fig. 2(b). The optical field is localized at the periphery of the microdisk and can couple to a tapered fiber evanescently.

The microdisk ultrasound sensors are characterized using the setup shown in Fig. 2(c). A continuous wave tunable laser in the 1550 nm band is used to couple light into the microdisk via a tapered fiber with a diameter of around 1 μm . The transmitted light from the tapered fiber is collected by a photodetector and subsequently measured by an oscilloscope, electronic spectrum analyzer (ESA), and vector network analyzer (VNA), respectively. By analyzing the transmitted light, the mechanical and optical modes of the microdisk, as well as its ultrasound response, can be obtained. The oscilloscope measures the optical transmission spectrum of the microdisk as the laser wavelength is scanned. The optical Q factors of microdisks can be derived from the optical transmission spectrum. A typical transmission spectrum at the critical-coupled condition is shown in Fig. 2(d), exhibiting an intrinsic optical Q factor of approximately 10^6 .

During the ultrasound detection experiments, an input optical power of around 100 μW is used, which is close to the saturation power of the photodetector. The critical-coupled condition between the tapered fiber and the microdisk is maintained to maximize the response. It is essential to lock the laser wavelength at the maximum slope on one side of the optical resonance to obtain the maximum optical readout. We employ

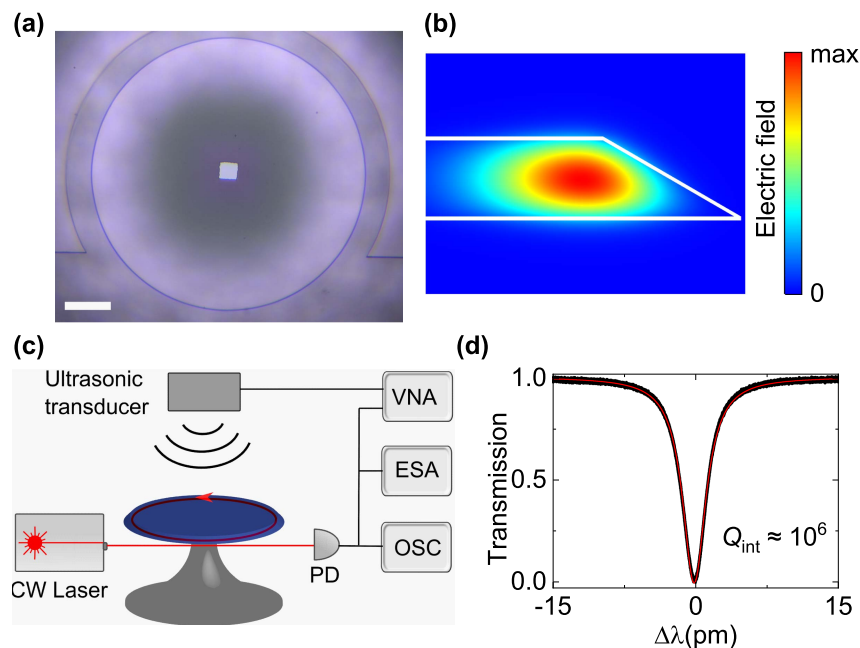


Fig. 2. (a) Top-view optical microscope image of a microdisk with a trench structure. The scale bar corresponds to 50 μm . (b) FEM simulated optical field distribution of the fundamental WGM of the microdisk. (c) Experimental setup to measure the microdisk response to ultrasound. PD, photodetector; VNA, vector network analyzer; OSC, oscilloscope; ESA, electronic spectrum analyzer. (d) Optical transmission spectrum of the microdisk, with an intrinsic Q factor of around 10^6 .

a proportional-integral-derivative controller to stabilize the laser wavelength. With the laser wavelength locked, the mechanical mode spectrum of the microdisk, as well as the ultrasound response spectrum, can be measured with the ESA and VNA. An ultrasonic transducer with a center frequency of 1 MHz is positioned approximately 1 cm above the microdisk. The ultrasound pressure generated by the ultrasonic transducer, ranging from 30 kHz to 20 MHz, is calibrated using the method presented in our previous work [22], taking into account the ultrasound attenuation in the air.

The optomechanical interaction in our system is a combination of dispersive and dissipative coupling. Ultrasound can cause variations in the microdisk circumference, which can shift the resonance wavelengths of the optical modes, resulting in a change in the transmitted optical power due to dispersive coupling. Additionally, ultrasound can also induce periodic changes in the coupling strength between the tapered fiber and the microdisk by varying the gap between them. This leads to a periodic modulation in the transmitted optical power, which is due to dissipative coupling. By locking the laser wavelength on one side of the optical resonance, we can measure both dispersive and dissipative interactions through the change in transmitted optical power.

4. RESULTS

In the experimental optimization of the ultrasound sensitivity, we achieve the best sensitivity of $1.18 \mu\text{Pa Hz}^{-1/2}$ utilizing a microdisk with a radius of $300 \mu\text{m}$ and a thickness of $2 \mu\text{m}$. The noise power spectrum obtained by the ESA without the ultrasound signal is shown in the black curve in Fig. 3(a). A mechanical resonance peak at $\Omega/2\pi = 83 \text{ kHz}$ is observed, which corresponds to the second-order flapping mode of the microdisk. The first-order flapping mode, which is not displayed here, occurs around 20 kHz and is outside the frequency range for ultrasound pressure calibration using our hydrophone. We also observe several mechanical modes of the tapered fiber within the frequency range below 30 kHz. The fitted mechanical Q factor is about 140. We then apply a sinusoidal voltage at this frequency to drive the ultrasonic transducer and measure the ultrasound response of the microdisk, as illustrated by the green curve in Fig. 3(a). The signal-to-noise ratio (SNR) at the peak is 58.73 dB. The sensitivity at 83 kHz is given by the following equation:

$$P_{\min}(\Omega) = P_{\text{applied}}(\Omega) \sqrt{\frac{1}{\text{SNR}} \frac{1}{\Delta f}} \quad (2)$$

P_{applied} represents the ultrasound pressure reaching the microdisk at 83 kHz, which is calibrated to be 6.12 mPa, while Δf represents the resolution bandwidth of the ESA, which is 30 Hz. The sensitivity at 83 kHz can be calculated as $1.29 \mu\text{Pa Hz}^{-1/2}$. In Fig. 3(a), we also observe a second-order mechanical sideband of the signal at 166 kHz, which originates from the nonlinear response of the optical readout mechanism [22]. Next, we measure the system response of the microdisk by sweeping the frequency of the applied ultrasonic wave using the VNA. Figure 3(b) shows the response spectrum of the

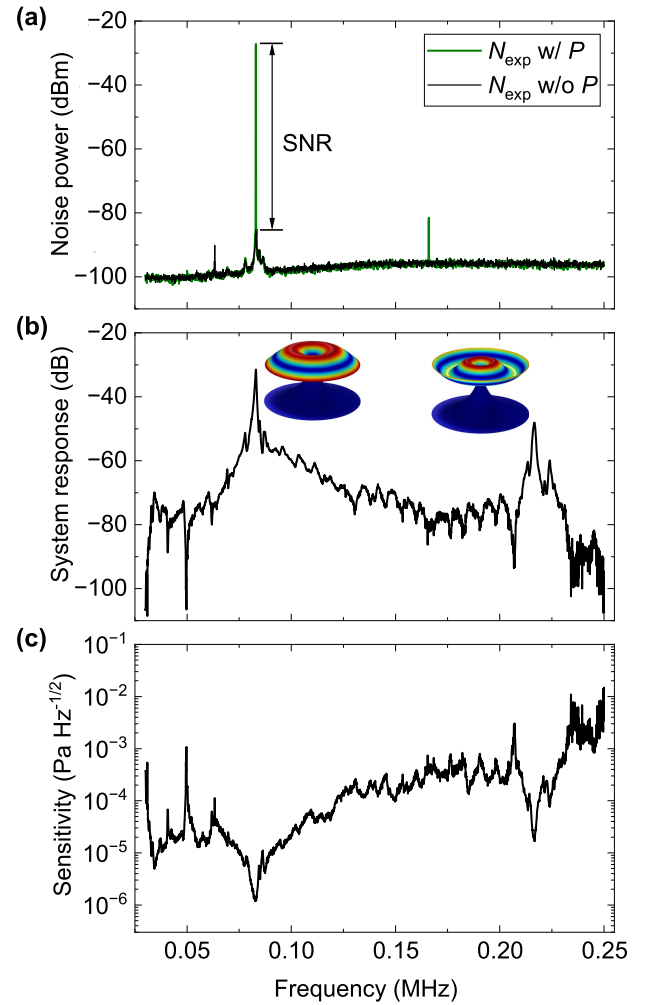


Fig. 3. (a) Noise power spectrum (black curve) and the response of the microdisk (green curve) driven by ultrasound at 83 kHz, with an SNR of 58.73 dB. (b) System response of the microdisk versus the ultrasound frequency. The inset shows the simulated displacement distributions of the high-order flapping modes. (c) Derived ultrasound sensitivity spectrum of the microdisk.

microdisk to ultrasound at different frequencies. In addition to the second-order flapping mode, we also observe another response peak corresponding to the third-order flapping mode at 216.6 kHz. Although this mode does not reach the thermal-noise-dominant regime and is not prominently shown in the noise power spectrum, we can still observe it in the system response due to the strong response of flapping modes to ultrasound. The sensitivity at different frequencies can be calculated using the following equation:

$$P_{\min}(\omega) = P_{\min}(\Omega) \frac{P_{\text{applied}}(\omega)}{P_{\text{applied}}(\Omega)} \sqrt{\frac{N(\omega) S(\Omega)}{N(\Omega) S(\omega)}}, \quad (3)$$

where $P_{\text{applied}}(\omega)$ represents the applied ultrasound pressure to the microdisk at different frequencies. By using the sensitivity at 83 kHz obtained above, along with the system response $S(\omega)$ and the noise power spectral density $N(\omega)$, we can derive the sensitivity spectrum of this microdisk for the entire frequency

range. This sensitivity describes the lowest detectable ultrasound pressure of the microdisk for a resolution bandwidth of 1 Hz when the SNR is 1. Figure 3(c) displays the sensitivity spectrum within the range of 0.03–0.25 MHz. A minimum sensitivity of $1.18 \mu\text{Pa Hz}^{-1/2}$ is achieved at 82.6 kHz, which is quite close to the theoretical value of $751 \text{ nPa Hz}^{-1/2}$ obtained from Eq. (1), using the pressure difference of 4.7 and the spatial overlap of 0.16.

To validate the theoretical results calculated above, we measured the sensitivities of multiple microdisks with varying radii and thicknesses. Figures 4(a) and 4(b) show the pressure sensitivity spectra near frequencies around the first- and second-order flapping modes for $1 \mu\text{m}$ thick microdisks with different radii. Figures 4(c)–4(e) present the data for microdisks with $2 \mu\text{m}$ thickness. The blue, red, black, green, and purple curves represent the sensitivities of microdisks with radii of $100 \mu\text{m}$, $150 \mu\text{m}$, $200 \mu\text{m}$, $300 \mu\text{m}$, and $400 \mu\text{m}$, for both $1 \mu\text{m}$ and $2 \mu\text{m}$ thicknesses. The $1 \mu\text{m}$ thick microdisks with a radius of $300 \mu\text{m}$ or larger have cracked during the XeF_2 dry etching process due to the material stress. Mechanical resonances of microdisks can significantly enhance their response to ultrasound,

resulting in numerous dips at mechanical resonance frequencies throughout the pressure sensitivity spectra. The widths of these dips, which represent the detection bandwidths, are determined by the thermal-noise-limited frequency range, which can be increased using microdisks with higher optical Q factors. Flapping modes, being more sensitive to ultrasound, generally exhibit better sensitivity. The shaded areas emphasize the sensitivities around the first-order [Figs. 4(a) and 4(c)] and second-order [Figs. 4(b), 4(d), and 4(e)] flapping modes.

From Fig. 4, we can observe that at a specific thickness, the mechanical resonance frequencies decrease with the increasing radius for both the first- and second-order flapping modes. For microdisks with the same radius, thinner ones exhibit lower frequencies for the first- and second-order flapping modes, which is consistent with theoretical results. For a more explicit comparison, we summarize the minimum sensitivity at the first- and second-order flapping modes in Fig. 5. The sensitivity for the first-order flapping mode improves with the increasing radius and the decreasing thickness of the microdisk. There is an anomaly where the sensitivity of the $1 \mu\text{m}$ thick microdisk with a radius of $100 \mu\text{m}$ is worse than that of the $2 \mu\text{m}$ thick

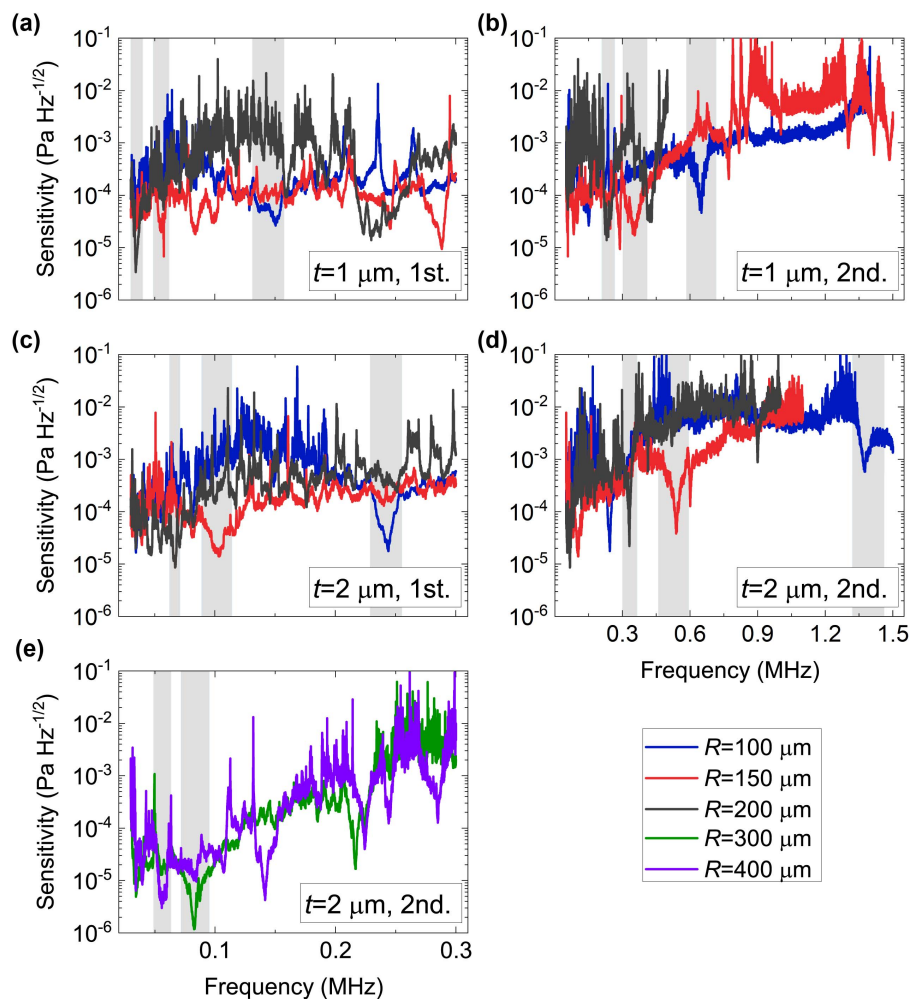


Fig. 4. (a), (b) Sensitivity spectra for $1 \mu\text{m}$ thick microdisks with different radii. (c)–(e) Sensitivity spectra for $2 \mu\text{m}$ thick microdisks with different radii. The blue, red, black, green, and purple curves represent the sensitivities of microdisks with radii of $100 \mu\text{m}$, $150 \mu\text{m}$, $200 \mu\text{m}$, $300 \mu\text{m}$, and $400 \mu\text{m}$, respectively. The shaded regions emphasize the (a), (c) first-order and (b), (d), (e) second-order flapping modes.

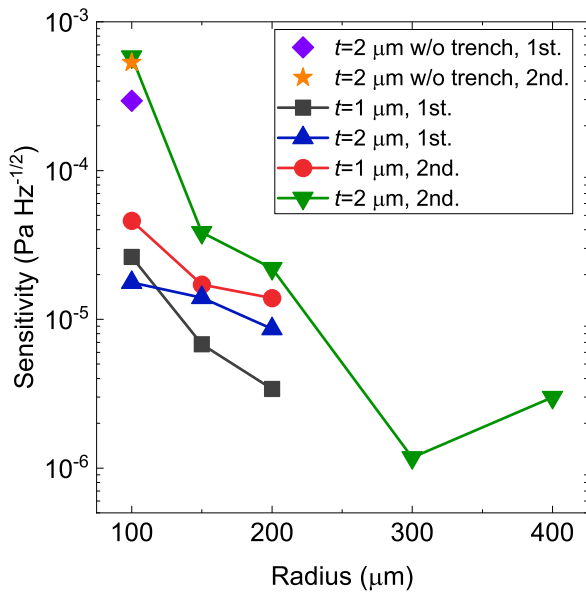


Fig. 5. Sensitivities at the flapping modes of microdisks with different thicknesses and radii. The black squares and blue triangles represent the sensitivities at the first-order flapping mode for thicknesses of 1 μm and 2 μm , respectively. The red circles and green inverted triangles represent sensitivities at the second-order flapping mode for thicknesses of 1 μm and 2 μm , respectively. The purple rhombus and yellow pentagram represent sensitivities at the first- and second-order flapping modes for a microdisk with a thickness of 2 μm and a radius of 100 μm , and without the trench structure.

microdisk, which may be attributed to their different mechanical Q factors and pressure differences. The sensitivity for the second-order flapping mode improves with the decreasing thickness of the microdisk. For the second-order flapping modes of the 2 μm thick microdisks, the sensitivity first improves with the increasing radius and reaches the optimal value of $1.18 \mu\text{Pa Hz}^{-1/2}$ for the microdisk with a radius of 300 μm . When the disk radius further increases to 400 μm , the sensitivity degrades to $2.99 \mu\text{Pa Hz}^{-1/2}$ due to the smaller pressure difference caused by the lower resonance frequency. We also measure a microdisk with a thickness of 2 μm and a radius of 100 μm without a trench structure, whose sensitivities at the first- and second-order flapping modes are shown in the purple rhombus and yellow pentagram in Fig. 5. Comparing these values with those of a same-sized microdisk with a trench structure (green inverted triangles and blue triangles) reveals that the trench structure significantly improves the sensitivity of the first-order flapping mode but does not affect the sensitivity at the second-order flapping mode. This is consistent with the theoretical results in Figs. 1(c)–1(f).

5. CONCLUSION

In conclusion, we have theoretically and experimentally studied the sensitivity of the microdisk ultrasound sensors in the thermal-noise-dominant regime. Our theoretical results show that the ultrasound sensitivity can be optimized by increasing the radius and decreasing the thickness of the microdisk but is also

Table 1. Comparison of WGM Microcavity Ultrasound Sensors

Structure	Q Factor	Sensitivity ($\mu\text{Pa Hz}^{-1/2}$)	References
Microsphere	$>10^8$	267	[9]
Microsphere	$\sim 10^6$	1.29×10^3	[10]
Microring	$\sim 10^4$	1.3×10^3	[16]
Microbubble	$\sim 10^7$	41×10^3	[17]
Microbubble	3×10^7	4.4×10^3	[19]
Microbubble	5.2×10^5	2.2×10^3	[20]
Microdisk	3.6×10^6	8–300	[21]
Microtoroid	$\sim 10^7$	46–10,000	[22]
Microdisk (this work)	$\sim 10^6$	1.18	—

affected by the pressure difference. We also find that using a trench structure around the microdisk can increase the pressure difference and, thereby, improve the sensitivity. We fabricate multiple microdisks with different radii (100 μm , 150 μm , 200 μm , 300 μm , and 400 μm) and thicknesses (1 μm and 2 μm) with trench structures, and characterized their ultrasound sensitivities. The measured sensitivity trends versus the radius and thickness agree well with the theoretical results. After optimization, a minimum sensitivity of $1.18 \mu\text{Pa Hz}^{-1/2}$ has been achieved at 82.6 kHz in the air, using a microdisk with a radius of 300 μm and a thickness of 2 μm . Table 1 compares structures, optical Q factors, and sensitivities of various WGM microcavity ultrasound sensors. As seen from the table, we have achieved the best ultrasound sensitivity among the WGM microcavity systems to the best of our knowledge. This is made possible by exploiting the optical and mechanical dual-resonance enhancement and optimizing the microdisk parameters.

The exceptional ultrasound sensitivity achieved in this study can extend the detection range of ultrasound detection technology, such as increasing the detection depth of photoacoustic imaging. It is particularly helpful for ultrasound detection in the air, which has proven challenging due to impedance mismatch. Furthermore, the fabrication process of microdisks is relatively mature, enabling mass production on silicon chips. The bandwidth of the ultrasound sensor can be further improved by using microcavities with higher optical Q factors and optomechanical coupling coefficients. Integrated waveguide-coupled microcavities and on-chip arrays of ultrasound sensors, such as silicon nitride and silicon microcavity sensors, can be designed in the future for practical applications, including photoacoustic imaging and spectroscopy.

Funding. National Key Research and Development Program of China (2021YFA1400700); National Natural Science Foundation of China (11934019, 12174438, 62222515, 91950118); Basic Frontier Science Research Program of Chinese Academy of Sciences (ZDBS-LY-JSC003).

Acknowledgment. The authors thank Prof. Yun-Feng Xiao for help with the calibration of the ultrasound pressure. This work was also supported by the Micro/nano Fabrication Laboratory of Synergetic Extreme Condition User Facility (SECUF).

Disclosures. The authors declare no conflicts of interest.

Data Availability. Data underlying the results presented in this paper are not publicly available at this time but may be obtained from the authors upon reasonable request.

REFERENCES

- R. Kotzé, S. Ricci, B. Birkhofer, and J. Wiklund, "Performance tests of a new non-invasive sensor unit and ultrasound electronics," *Flow Meas. Instrum.* **48**, 104–111 (2016).
- A. P. Rao, N. Bokde, and S. Sinha, "Photoacoustic imaging for management of breast cancer: a literature review and future perspectives," *Appl. Sci.* **10**, 767 (2020).
- A. De Angelis, A. Moschitta, P. Carbone, M. Calderini, S. Neri, R. Borgna, and M. Peppucci, "Design and characterization of a portable ultrasonic indoor 3-D positioning system," *IEEE Trans. Instrum. Meas.* **64**, 2616–2625 (2015).
- J. Ma, H. Xuan, H. L. Ho, W. Jin, Y. Yang, and S. Fan, "Fiber-optic Fabry-Pérot acoustic sensor with multilayer graphene diaphragm," *IEEE Photon. Technol. Lett.* **25**, 932–935 (2013).
- F. Xu, J. Shi, K. Gong, H. Li, R. Hui, and B. Yu, "Fiber-optic acoustic pressure sensor based on large-area nanolayer silver diaphragm," *Opt. Lett.* **39**, 2838–2840 (2014).
- J. A. Guggenheim, J. Li, T. J. Allen, R. J. Colchester, S. Noimark, O. Ogunlade, I. P. Parkin, I. Papakonstantinou, A. E. Desjardins, E. Z. Zhang, and P. C. Beard, "Ultrasensitive plano-concave optical microresonators for ultrasound sensing," *Nat. Photonics* **11**, 714–719 (2017).
- G. J. Hornig, K. G. Scheuer, E. B. Dew, R. Zemp, and R. G. DeCorby, "Ultrasound sensing at thermomechanical limits with optomechanical buckled-dome microcavities," *Opt. Express* **30**, 33083–33096 (2022).
- M. V. Chistiakova and A. M. Armani, "Photoelastic ultrasound detection using ultra-high-Q silica optical resonators," *Opt. Express* **22**, 28169–28179 (2014).
- J. Yang, T. Qin, F. Zhang, X. Chen, X. Jiang, and W. Wan, "Multiphysical sensing of light, sound and microwave in a microcavity Brillouin laser," *Nanophotonics* **9**, 2915–2925 (2020).
- J.-W. Meng, S.-J. Tang, J. Sun, K. Shen, C. Li, Q. Gong, and Y.-F. Xiao, "Dissipative acousto-optic interactions in optical microcavities," *Phys. Rev. Lett.* **129**, 073901 (2022).
- J. Sun, J.-W. Meng, S.-J. Tang, and C. Li, "An encapsulated optical microsphere sensor for ultrasound detection and photoacoustic imaging," *Sci. China Phys. Mech. Astron.* **65**, 224211 (2021).
- C. Zhang, T. Ling, S.-L. Chen, and L. J. Guo, "Ultrabroad bandwidth and highly sensitive optical ultrasonic detector for photoacoustic imaging," *ACS Photon.* **1**, 1093–1098 (2014).
- H. Li, B. Dong, Z. Zhang, H. F. Zhang, and C. Sun, "A transparent broadband ultrasonic detector based on an optical micro-ring resonator for photoacoustic microscopy," *Sci. Rep.* **4**, 4496 (2014).
- S. M. Leinders, W. J. Westerveld, J. Pozo, P. L. M. J. van Neer, B. Snyder, P. O'Brien, H. P. Urbach, N. de Jong, and M. D. Verweij, "A sensitive optical micro-machined ultrasound sensor (OMUS) based on a silicon photonic ring resonator on an acoustical membrane," *Sci. Rep.* **5**, 14328 (2015).
- H. Li, B. Dong, X. Zhang, X. Shu, X. Chen, R. Hai, D. A. Czaplowski, H. F. Zhang, and C. Sun, "Disposable ultrasound-sensing chronic cranial window by soft nanoimprinting lithography," *Nat. Commun.* **10**, 4277 (2019).
- W. J. Westerveld, M. Mahmud-UI-Hasan, R. Shnaiderman, V. Ntziachristos, X. Rottenberg, S. Severi, and V. Rochus, "Sensitive, small, broadband and scalable optomechanical ultrasound sensor in silicon photonics," *Nat. Photonics* **15**, 341–345 (2021).
- K. H. Kim, W. Luo, C. Zhang, C. Tian, L. J. Guo, X. Wang, and X. Fan, "Air-coupled ultrasound detection using capillary-based optical ring resonators," *Sci. Rep.* **7**, 109 (2017).
- G. Frigenti, L. Cavigli, A. Fernández-Bienes, F. Ratto, S. Centi, T. Garca-Fernández, G. Nunzi Conti, and S. Soria, "Resonant microbubble as a microfluidic stage for all-optical photoacoustic sensing," *Phys. Rev. Appl.* **12**, 014062 (2019).
- J. Pan, B. Zhang, Z. Liu, J. Zhao, Y. Feng, L. Wan, and Z. Li, "Microbubble resonators combined with a digital optical frequency comb for high-precision air-coupled ultrasound detectors," *Photon. Res.* **8**, 303–310 (2020).
- X. Tu, Y. Wang, Z. Guo, Z. Chen, T. Huang, X. Wu, and W. Luo, "Underwater acoustic wave detection based on packaged optical microbubble resonator," *J. Lightwave Technol.* **40**, 6272–6279 (2022).
- S. Basiri-Esfahani, A. Armin, S. Forstner, and W. P. Bowen, "Precision ultrasound sensing on a chip," *Nat. Commun.* **10**, 132 (2019).
- H. Yang, Z.-G. Hu, Y. Lei, X. Cao, M. Wang, J. Sun, Z. Zuo, C. Li, X. Xu, and B.-B. Li, "High-sensitivity air-coupled megahertz-frequency ultrasound detection using on-chip microcavities," *Phys. Rev. Appl.* **18**, 034035 (2022).
- R. Shnaiderman, G. Wissmeyer, O. Ülgen, Q. Mustafa, A. Chmyrov, and V. Ntziachristos, "A submicrometre silicon-on-insulator resonator for ultrasound detection," *Nature* **585**, 372–378 (2020).
- Y. Hazan, A. Levi, M. Nagli, and A. Rosenthal, "Silicon-photonics acoustic detector for optoacoustic micro-tomography," *Nat. Commun.* **13**, 1488 (2022).
- K. J. Vahala, "Optical microcavities," *Nature* **424**, 839–846 (2003).
- D. K. Armani, T. J. Kippenberg, S. M. Spillane, and K. J. Vahala, "Ultra-high-Q toroid microcavity on a chip," *Nature* **421**, 925–928 (2003).
- J. Liu, F. Bo, L. Chang, C.-H. Dong, X. Ou, B. Regan, X. Shen, Q. Song, B. Yao, W. Zhang, C.-L. Zou, and Y.-F. Xiao, "Emerging material platforms for integrated microcavity photonics," *Sci. China Phys. Mech. Astron.* **65**, 104201 (2022).
- J. Liao and L. Yang, "Optical whispering-gallery mode barcodes for high-precision and wide-range temperature measurements," *Light Sci. Appl.* **10**, 32 (2021).
- M.-G. Suh, Q.-F. Yang, K. Y. Yang, X. Yi, and K. J. Vahala, "Microresonator soliton dual-comb spectroscopy," *Science* **354**, 600–603 (2016).
- J. M. Ward, Y. Yang, F. Lei, X.-C. Yu, Y.-F. Xiao, and S. N. Chormaic, "Nanoparticle sensing beyond evanescent field interaction with a quasi-droplet microcavity," *Optica* **5**, 674–677 (2018).
- X.-C. Yu, S.-J. Tang, W. Liu, Y. Xu, Q. Gong, Y.-L. Chen, and Y.-F. Xiao, "Single-molecule optofluidic microsensor with interface whispering gallery modes," *Proc. Natl. Acad. Sci. U.S.A.* **119**, e2108678119 (2022).
- J. Zhu, S. K. Ozdemir, Y.-F. Xiao, L. Li, L. He, D.-R. Chen, and L. Yang, "On-chip single nanoparticle detection and sizing by mode splitting in an ultrahigh-Q microresonator," *Nat. Photonics* **4**, 46–49 (2010).
- L. He, Ş. K. Özdemir, J. Zhu, W. Kim, and L. Yang, "Detecting single viruses and nanoparticles using whispering gallery microlasers," *Nat. Nanotechnol.* **6**, 428–432 (2011).
- L. Shao, X.-F. Jiang, X.-C. Yu, B.-B. Li, W. R. Clements, F. Vollmer, W. Wang, Y.-F. Xiao, and Q. Gong, "Detection of single nanoparticles and lentiviruses using microcavity resonance broadening," *Adv. Mater.* **25**, 5616–5620 (2013).
- B.-B. Li, W. R. Clements, X.-C. Yu, K. Shi, Q. Gong, and Y.-F. Xiao, "Single nanoparticle detection using split-mode microcavity Raman lasers," *Proc. Natl. Acad. Sci. U.S.A.* **111**, 14657–14662 (2014).
- Ş. K. Özdemir, J. Zhu, X. Yang, B. Peng, H. Yilmaz, L. He, F. Monifi, S. H. Huang, G. L. Long, and L. Yang, "Highly sensitive detection of nanoparticles with a self-referenced and self-heterodyned whispering-gallery Raman microlaser," *Proc. Natl. Acad. Sci. USA* **111**, E3836–E3844 (2014).
- M. Jin, S.-J. Tang, J.-H. Chen, X.-C. Yu, H. Shu, Y. Tao, A. K. Chen, Q. Gong, X. Wang, and Y.-F. Xiao, "1/f-noise-free optical sensing with an integrated heterodyne interferometer," *Nat. Commun.* **12**, 1973 (2021).
- Y. Zhi, X.-C. Yu, Q. Gong, L. Yang, and Y.-F. Xiao, "Single nanoparticle detection using optical microcavities," *Adv. Mater.* **29**, 1604920 (2017).
- R. Niu, M. Li, S. Wan, Y. R. Sun, S.-M. Hu, C.-L. Zou, G.-C. Guo, and C.-H. Dong, "kHz-precision wavemeter based on reconfigurable microsolviton," *Nat. Commun.* **14**, 169 (2023).

40. D.-Q. Yang, J.-H. Chen, Q.-T. Cao, B. Duan, H.-J. Chen, X.-C. Yu, and Y.-F. Xiao, "Operando monitoring transition dynamics of responsive polymer using optofluidic microcavities," *Light Sci. Appl.* **10**, 128 (2021).
41. D. Yang, A. Wang, J.-H. Chen, X.-C. Yu, C. Lan, Y. Ji, and Y.-F. Xiao, "Real-time monitoring of hydrogel phase transition in an ultrahigh microbubble resonator," *Photon. Res.* **8**, 497–502 (2020).
42. M. Aspelmeyer, T. J. Kippenberg, and F. Marquardt, "Cavity optomechanics," *Rev. Mod. Phys.* **86**, 1391–1452 (2014).
43. T. J. Kippenberg and K. J. Vahala, "Cavity optomechanics: back-action at the mesoscale," *Science* **321**, 1172–1176 (2008).
44. M. Metcalfe, "Applications of cavity optomechanics," *Appl. Phys. Rev.* **1**, 031105 (2014).
45. B.-B. Li, J. Bílek, U. B. Hoff, L. S. Madsen, S. Forstner, V. Prakash, C. Schäfermeier, T. Gehring, W. P. Bowen, and U. L. Andersen, "Quantum enhanced optomechanical magnetometry," *Optica* **5**, 850–856 (2018).
46. B.-B. Li, G. Brawley, H. Greenall, S. Forstner, E. Sheridan, H. Rubinsztein-Dunlop, and W. P. Bowen, "Ultrabroadband and sensitive cavity optomechanical magnetometry," *Photon. Res.* **8**, 1064–1071 (2020).
47. J. Li, Z.-H. Zhou, S. Wan, Y.-L. Zhang, Z. Shen, M. Li, C.-L. Zou, G.-C. Guo, and C.-H. Dong, "All-optical synchronization of remote optomechanical systems," *Phys. Rev. Lett.* **129**, 063605 (2022).
48. G.-T. Xu, Z. Shen, Y. Wang, C.-Z. Chai, G.-C. Guo, and C.-H. Dong, "Optomechanical magnetometry on a bubble resonator with YIG microsphere," *IEEE Photon. Technol. Lett.* **35**, 393–396 (2023).
49. M. Sansa, M. Defoort, A. Brenac, M. Hermouet, L. Banniard, A. Fafin, M. Gely, C. Masselon, I. Favero, G. Jourdan, and S. Hentz, "Optomechanical mass spectrometry," *Nat. Commun.* **11**, 3781 (2020).
50. E. Gavartin, P. Verlot, and T. J. Kippenberg, "A hybrid on-chip optomechanical transducer for ultrasensitive force measurements," *Nat. Nanotechnol.* **7**, 509–514 (2012).
51. H. Wu, L. Dong, H. Zheng, Y. Yu, W. Ma, L. Zhang, W. Yin, L. Xiao, S. Jia, and F. K. Tittel, "Beat frequency quartz-enhanced photoacoustic spectroscopy for fast and calibration-free continuous trace-gas monitoring," *Nat. Commun.* **8**, 15331 (2017).
52. B.-B. Li, L. Ou, Y. Lei, and Y.-C. Liu, "Cavity optomechanical sensing," *Nanophotonics* **10**, 2799–2832 (2021).